

ARTICLE OPEN



Coherent control of electron spin qubits in silicon using a global field

E. Vahapoglu¹✉, J. P. Slack-Smith¹✉, R. C. C. Leon¹, W. H. Lim^{1,2}, F. E. Hudson^{1,2}, T. Day¹, J. D. Cifuentes¹, T. Tanttu^{1,2}, C. H. Yang^{1,2}, A. Saraiva^{1,2}, N. V. Abrosimov³, H.-J. Pohl⁴, M. L. W. Thewalt⁵, A. Laucht^{1,2}✉, A. S. Dzurak^{1,2,6}✉ and J. J. Pla^{1,6}✉

Silicon spin qubits promise to leverage the extraordinary progress in silicon nanoelectronic device fabrication over the past half century to deliver large-scale quantum processors. Despite the scalability advantage of using silicon technology, realising a quantum computer with the millions of qubits required to run some of the most demanding quantum algorithms poses several outstanding challenges, including how to control many qubits simultaneously. Recently, compact 3D microwave dielectric resonators were proposed as a way to deliver the magnetic fields for spin qubit control across an entire quantum chip using only a single microwave source. Although spin resonance of individual electrons in the globally applied microwave field was demonstrated, the spins were controlled incoherently. Here we report coherent Rabi oscillations of single electron spin qubits in a planar SiMOS quantum dot device using a global magnetic field generated off-chip. The observation of coherent qubit control driven by a dielectric resonator establishes a credible pathway to achieving large-scale control in a spin-based quantum computer.

npj Quantum Information (2022)8:126; <https://doi.org/10.1038/s41534-022-00645-w>

INTRODUCTION

Quantum computers have the potential to transform our ability to solve currently intractable problems, with implications for critical sectors such as finance, defence and pharmaceuticals. The benefits of quantum computation are already expected to be observed with "noisy intermediate scale quantum" (NISQ) devices¹, which possess tens to hundreds of qubits. However, it is widely acknowledged that the algorithms² expected to provide the most significant advantage over their classical counterparts will require error correction, where information is encoded in logical qubits and processors need millions of physical qubits to operate^{3,4}. Scalability is thus an unavoidable objective for any quantum computation technology platform.

Electron spin qubits in gate-defined silicon quantum dot (QD) devices are a leading platform for realising large-scale quantum computers. Silicon QDs exhibit relatively long coherence times⁵, are able to operate at temperatures above 1 K^{6,7}, and can utilise traditional very large-scale integration (VLSI) fabrication processes^{8,9}. The feasibility of universal quantum computing in silicon has been established through the demonstration of high-fidelity single^{5,10,11} and two^{12–14} qubit gates, with the focus now on scaling up to NISQ devices and beyond to fault-tolerant systems⁸.

A critical requirement along this path is the ability to deliver microwave signals, which are needed to control spin qubits, across the entire quantum chip. Current methods for controlling electron spin qubits in devices include direct magnetic driving using on-chip transmission lines (TL)^{15,16} and electrically driven spin resonance (EDSR)^{6,17–21}, both of which have proven useful in small scale (1–10 qubit) device demonstrations. However, as the number of qubits scales up, heating and design complexity issues will need to be resolved^{22,23} for these approaches to be practical.

Global control²⁴ was an early technique proposed for spin qubits, offering a scalable solution to the problem of delivering microwave signals. Here, a global and uniform magnetic field is

applied across the entire quantum chip in order to drive each qubit^{8,25,26}. Qubit manipulation is activated by locally applied electric fields to shift their individual resonance frequencies into and out of resonance with the global field²⁷. This technique differs from the well-established TL¹⁵ and EDSR¹⁷-based approaches by applying a single microwave field to all qubits (potentially millions²⁶) in the quantum processor, instead of just a few. It does not suffer the same scalability concerns as those approaches, since no high frequency lines or microwave currents directly pass through the chip.

Despite the appeal of global control, owing to its simplicity, single spin resonance using a global field was only achieved recently. A 3D microwave dielectric resonator (DR) made from potassium tantalate (KTaO₃ or KTO)^{26,28,29} was used to create a global, off-chip magnetic field and perform electron spin resonance (ESR) of single spins in a planar SiMOS device²⁶. The microwave magnetic field generated by the DR produced incoherent mixing of spin states in a double quantum dot (DQD), which was detected with a single electron transistor through a process known as spin to charge conversion³⁰. However, the coherent control of spin qubits using a global field has remained an outstanding challenge that must be addressed to fully establish the feasibility of applying this technique in large-scale quantum computers.

Here we present the coherent control of single electron spin qubits in a planar SiMOS DQD device using a global magnetic microwave field generated off-chip by a KTO dielectric resonator. We measure Rabi frequencies and report on the coherence properties of both spin qubits. We compare the noise spectrum seen by the qubits in this DR-driven device to that observed by traditional TL-driven qubits and conclude that this new scalable approach does not diminish the performance of the qubits. This work demonstrates the potential of global control using dielectric resonators as a scalable qubit control technique.

¹School of Electrical Engineering and Telecommunications, UNSW Sydney, Sydney, NSW 2052, Australia. ²Diraq, Sydney, NSW, Australia. ³Leibniz-Institut für Kristallzüchtung, 12489 Berlin, Germany. ⁴VITCON Projectconsult GmbH, 07745 Jena, Germany. ⁵Department of Physics, Simon Fraser University, Burnaby, BC V5A 1S6, Canada. ⁶These authors contributed equally: A. S. Dzurak, J. J. Pla. ✉email: e.vahapoglu@unsw.edu.au; j.slack-smith@unsw.edu.au; a.dzurak@unsw.edu.au; jarryd@unsw.edu.au

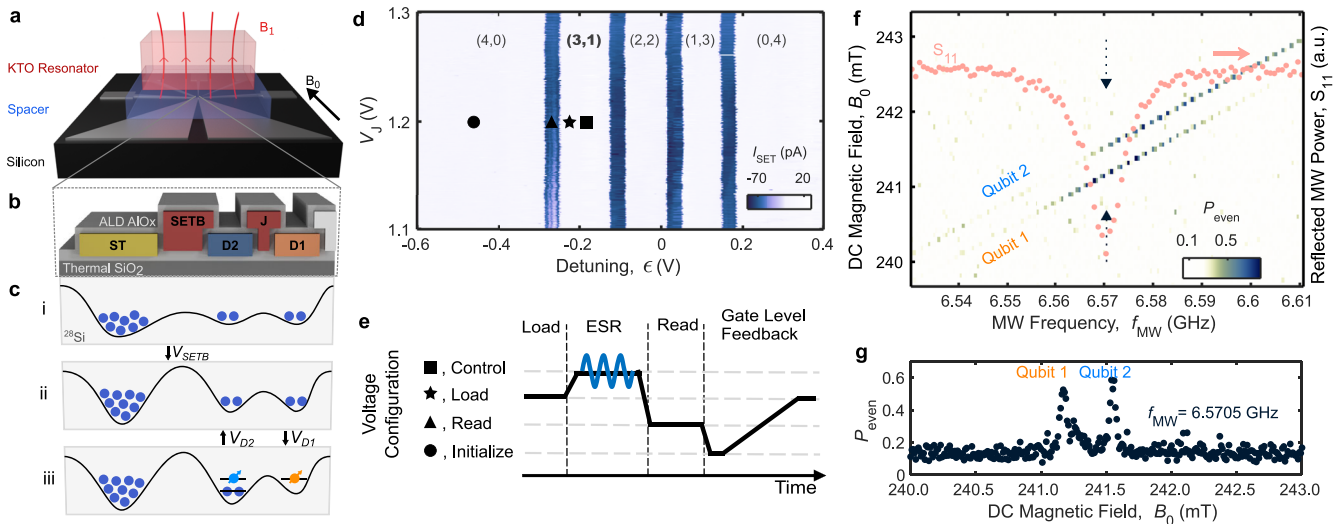


Fig. 1 Device stack and electron spin resonance (ESR). **a** A 3D render of the global control device stack used in our experiments, including the silicon quantum nanoelectronic device (bottom, black), sapphire dielectric spacer (middle, blue) and potassium tantalate (KTO) dielectric microwave resonator (top, pink). **b** A schematic cross-section through the measured silicon QD device showing the 3D structure of the gates, enriched silicon-28 substrate (merged with panel **c**) and insulating oxide layers. **c** Steps for preparing the isolated mode measurements, depicted with conduction band profiles at the interface of the ^{28}Si substrate. The preparation consists of three phases: loading (i), isolation (ii) and initialisation (iii) (see text for more details). **d** Charge stability diagram measured in isolated mode. Four charge transitions occur while the detuning voltage ϵ is swept from -0.6 to 0.4 V, indicating that there are 4 electrons in the double dot system. Black geometric symbols (explained in panel **e**) show the voltage configurations used in the ESR experiments. **e** Pulsing scheme for the ESR measurements. For a detailed explanation, please see Methods. **f** Even state probability as a function of f_{MW} and B_0 , revealing two ESR peaks that shift with magnetic field, consistent with two spin qubits occupying the double dot system. The peaks are labelled Qubit 1 and Qubit 2. An S_{11} reflection measurement (pink circles) probed via the coaxial loop coupler is superimposed over the 2D map. The ESR pulse duration is fixed at $1.5 \mu\text{s}$. **g** Even state probability as a function of B_0 when f_{MW} corresponds to the centre frequency of the DR resonance (dotted lines with arrows in panel **f**). The pulse duration is sufficiently long to make the ESR drive incoherent ($25\mu\text{s}$), causing the spin states to become completely mixed and resulting in a peak amplitude of $P_{\text{even}} = 0.5$ for both resonances.

RESULTS

Single spin resonance

The device studied here employs a nominally identical stack as reported previously²⁶ (see Fig. 1a), which consists of a $0.7 \times 0.55 \times 0.3$ mm rectangular KTO prism positioned above a silicon quantum nanoelectronic device. A 0.2 mm thick low-loss dielectric sapphire spacer is positioned between the DR and device to isolate them from one another. The fundamental mode of the DR produces an alternating magnetic field (B_1) out of the qubit plane and in a direction perpendicular to the DC magnetic field (B_0), as shown in Fig. 1a. We use the B_1 field to control the spin state of the qubits via magnetic resonance. A coaxial loop coupler, through which the microwave power is inductively coupled to the DR, is placed above the stack²⁶ (not shown).

The qubit device is a metal-oxide-semiconductor (MOS) DQD formed in an isotopically enriched silicon-28 substrate (50 ppm residual ^{29}Si), whose cross-sectional view is depicted in Fig. 1b. This is in contrast to previous work²⁶ which employed a natural silicon substrate with a $\sim 4.7\%$ abundance of ^{29}Si nuclei, which produced strong dephasing of the electron spins. Isotopic enrichment is a well-established technique for enhancing the coherence times of spin qubits in silicon devices^{31,32}. A scanning electron microscope (SEM) image of an identical device to the one measured is also provided in Supplementary Note 1. The QDs are electrostatically defined by a palladium (Pd) multi-layer gate stack architecture in which different layers are electrically isolated by atomic-layer-deposited (ALD) aluminium oxide (AlO_x), since Pd does not form its own native oxide³³. A thermally grown SiO_2 layer above the silicon substrate prevents any current leakage between the gate electrodes and the substrate. The device consists of a single electron transistor (SET), which is used as a charge sensor, with a top gate (ST) for tuning its charge accumulation and sensitivity, two plunger gates (D1–D2) for forming the quantum

dots and setting their charge occupations, two barrier gates that control the coupling between the dots (J) or between dot 2 and the SET island (SETB) and confinement gates (CB1–CB2) to laterally confine the dots (not shown in Fig. 1b, see the SEM image in the Supplementary Information).

Measurements in this work have been carried out in a configuration referred to here as *isolated mode*, where the electrons inside the double dot system are electrically isolated from the nearby electron reservoirs, as employed elsewhere⁶. The steps required to prepare this configuration are depicted in Fig. 1c and entail three main stages. In the loading phase (i), electrons are introduced to the double dot system via the SET, which is also coupled to an electron reservoir (not shown). The number of electrons loaded can be tuned using the D1, D2 and J gates. The system is then isolated (ii) by raising the potential underneath the gate SETB. Finally, the desired charge occupation is initialised (iii) by setting the plunger gate (D1 and D2) voltages appropriately. Figure 1d shows a charge stability diagram measured in isolated mode with a double lock-in technique³⁴. The four vertical blue lines indicate that 4 electrons are trapped inside the DQD system, with tunnelling between the dots depending on the value of the voltage detuning ($\epsilon = V_{D1} - V_{D2}$). A more positive ϵ favours electron occupation under gate D1, whilst a more negative ϵ favours occupation under D2. The absence of additional lines on both sides of the diagram (also not observed on a measurement over a larger V_J range, see Supplementary Fig. 3) confirm that only 4 electrons have been loaded in the DQD system. The charge configurations are labelled as (N2, N1) where N1(2) refers to the number of electrons under D1(2).

In the following spin measurements we focus on the (3,1) charge configuration (emphasised in Fig. 1d), which provides an equivalent spin state to (1,1) since the first two electrons under D2 form a spin-zero closed shell and do not interact with the remaining electrons in the system (see panel iii in Fig. 1c). This is

preferred rather than having only 2 electrons in total, since the orbital splitting is generally an order of magnitude larger than valley splitting in SiMOS devices³⁵. Figure 1e depicts the pulse scheme applied during the measurements. The system is first initialised in a spin singlet state $(|\downarrow\uparrow\rangle + |\uparrow\downarrow\rangle)/\sqrt{2}$ (see Supplementary Note 4). Following this, the system is plunged into the middle of the (3,1) region – and converted to a $|\downarrow\uparrow\rangle$ state—while a microwave signal is applied to the loop coupler for a period of time in order to flip the spins in the DQD with the global B_1 field. If the frequency of the B_1 field matches one of the qubit frequencies, i.e. $f_{\text{MW}} = g\mu_B B_0/h$ (where g is the electron g-factor, μ_B the Bohr magneton and h Planck's constant), the resonant spin qubit will flip between the $|\uparrow\rangle$ and $|\downarrow\rangle$ states. The resulting DQD spin state is then translated into a charge state in the Pauli Spin Blockade (PSB) region, measured using the SET, as either a singlet or triplet state³⁰. However, we have confirmed that the blockade is restricted to even parity spin states instead of all triplet states (in what is known as parity readout³⁶). Therefore, the readout effectively unveils an even or odd parity spin state.

In Fig. 1f we plot the measured DQD even state probability (P_{even}) after applying the measurement sequence (Fig. 1e), as we scan both the B_0 field and the microwave frequency f_{MW} . Electron spin resonance signatures are detected for the spins in both dots (diagonal features in Fig. 1f), where it is observed that the qubit frequencies shift linearly as a function of B_0 , confirming the features are indeed electron spin resonance (ESR) peaks. Note that for SiMOS spin qubit devices, the qubit frequencies are different due to the variability in spin-orbit effects caused by the imperfections (e.g. surface roughness) in the Si-SiO₂ interface³⁷. By monitoring how the qubit frequencies change due to Stark shifts from voltages applied to the different gates (see analysis in the Supplementary Note 5), we deduce that the spin resonance signal at the higher frequency (for a fixed B_0) corresponds to the spin under gate D1, whilst the other resonance belongs to the spin under D2. We thus label the resonances as 'Qubit 1' and 'Qubit 2', respectively. We perform an S_{11} reflection measurement on the dielectric resonator via the loop coupler and superimpose it on Fig. 1f (pink circles). The amplitude of the ESR peaks are correlated with the S_{11} DR resonance, indicating that the B_1 field generated by the KTO resonator indeed drives the qubits²⁶. In Fig. 1g we show a one-dimensional slice of the qubit resonances taken at the DR centre frequency, measured along the black dotted arrows marked in Fig. 1f.

These results are consistent with recent observations in a natural silicon device²⁶, confirming that this new spin control technology is device independent. Next, we exploit the long spin coherence times available in enriched ²⁸Si to enable coherent qubit control using the off-chip B_1 field.

Coherent qubit control

We measure the even state probability P_{even} as a function of the applied ESR pulse length (t_p), with f_{MW} and B_0 chosen to satisfy the resonance condition $f_{\text{MW}} = g\mu_B B_0/h$ for each qubit. The result is plotted in Fig. 2a and clearly demonstrates coherent Rabi oscillations. Repeating this measurement as a function of f_{MW} for a fixed B_0 (see Fig. 2b, c) we observe Rabi chevron patterns for both qubits, where faster driving occurs as f_{MW} becomes detuned from resonance with the qubits and is accompanied by a reduction in the oscillation visibility. The qubit frequency drifts seen in these Chevron patterns is a phenomenon commonly observed in spin qubit systems³⁸ and not specifically related to the physics of the dielectric cavity.

The relation between the B_1 field generated by the DR and the applied microwave power is given as $B_1 = C\sqrt{P_{\text{MW}}}$, where C is the conversion factor and P_{MW} is the power^{26,29}. Therefore, we expect $f_{\text{Rabi}} = g\mu_B B_1/h$ to have a linear dependence on $\sqrt{P_{\text{MW}}}$. This is investigated in Fig. 2d, where for low powers f_{Rabi} indeed increases

linearly with respect to $\sqrt{P_{\text{MW}}}$ with an average conversion factor extracted from the slopes of this plot of $C \approx 11 \mu\text{T}/\sqrt{\mu\text{W}}$.

For powers exceeding $P_{\text{MW}} \approx 20 \mu\text{W}$ (≈ -17 dBm) the Rabi frequency begins to saturate for both qubits. We probe the shift in the resonance frequency of the KTO resonator (relative to its low-power value) as a function of P_{MW} and find that the change is minimal (<1 MHz) over the range of powers measured, which would not suffice to explain the saturation as discussed below. We therefore conclude that the observed saturation in f_{Rabi} is not caused by power-induced shifts of the DR frequency, for example due to microwave heating of the KTO dielectric material²⁹. Qualitatively similar behaviour has been observed before in devices very different from the one investigated here, including devices with microwave drive applied by broadband on-chip antennae and made with different materials stacks (Aluminium gates with thermally oxidised insulation between the gates). While in some cases a small stray electric-field drive might be present (which is known to cause a saturation at high amplitudes³⁹), the underlying cause for the saturation of the magnetic drive remains unexplained. Further work is warranted to understand the mechanism behind the Rabi frequency saturation.

Next we explore how f_{Rabi} varies with respect to the qubit resonance frequencies (f_{qubit}) in order to quantify the effect of the resonator more accurately. We have measured Rabi oscillations for different f_{qubit} values (setting $B_0 = hf_{\text{qubit}}/g\mu_B$) around the fundamental mode of the DR, and plot f_{Rabi} against f_{qubit} for both qubits in Fig. 2e, f. It is clear from these measurements that f_{Rabi} is enhanced for qubit frequencies corresponding with the DR resonance (as can be seen from the superimposed S_{11} measurement), which implies that the qubits are primarily driven by the KTO resonator in these regions. Compared to the off-resonant drive, f_{Rabi} is enhanced at the centre of the DR resonance by a factor of 3.3 for Qubit 1 and 2 for Qubit 2. We note that a factor 3.3 enhancement in B_1 corresponds to a >10 times lower power requirement for a given field strength. There is also a residual drive that is present across all qubit frequencies, which we believe could originate from several sources. Microwaves may couple into a broadband transmission line (unused in this experiment, see Supplementary Fig. 2) that is terminated 200 nm from the DQD, producing a weak B_1 field across a large bandwidth. In addition, microwave currents that are induced in the metal gate electrodes may produce magnetic or electric fields that result in weak ESR or EDSR⁴⁰. Especially electric drive—combined with a location-dependent spin-orbit interaction strength⁴¹—could explain the frequency domain response differences between the qubits. See Supplementary Note 7 for additional data supporting this hypothesis. Finally, we note that the data in Fig. 2e, f also indicate that a <1 MHz shift from the DR resonance should result in a less than 5% drop in the Rabi frequency, which implies that the Rabi frequency saturation observed in Fig. 2d cannot be explained solely by the shift in resonator frequency.

Coherence time measurements

We investigate the coherence times of the qubits by performing Ramsey free induction decay and Hahn echo experiments. The data measured in these experiments are shown in Fig. 3a, b for Qubits 1 and 2, respectively. To extract the T_2^* times, we fit the Ramsey data to exponential decay functions of the form $P_{\text{even}} = Ae^{-(t/T_2^*)^n} + B$, where the parameters A and B are related to the measurement visibility and n is the decay exponent, typically ranging between 1 and 2 (ref. 42). The fits reveal $T_2^* = 2.33 \pm 0.35 \mu\text{s}$ ($n = 1.13$) for Qubit 1 and $T_2^* = 1.79 \pm 0.20 \mu\text{s}$ ($n = 1.27$) for Qubit 2. Similarly, the Hahn echo measurement results are fit with the function $P_{\text{even}} = A(1 - e^{-(t/T_2^{\text{Hahn}})^n}) + B$, yielding $T_2^{\text{Hahn}} = 9.5 \pm 1.0 \mu\text{s}$ ($n = 1.86$) for Qubit 1 and $T_2^{\text{Hahn}} = 12.1 \pm 1.4 \mu\text{s}$ ($n = 1.67$) for Qubit 2.

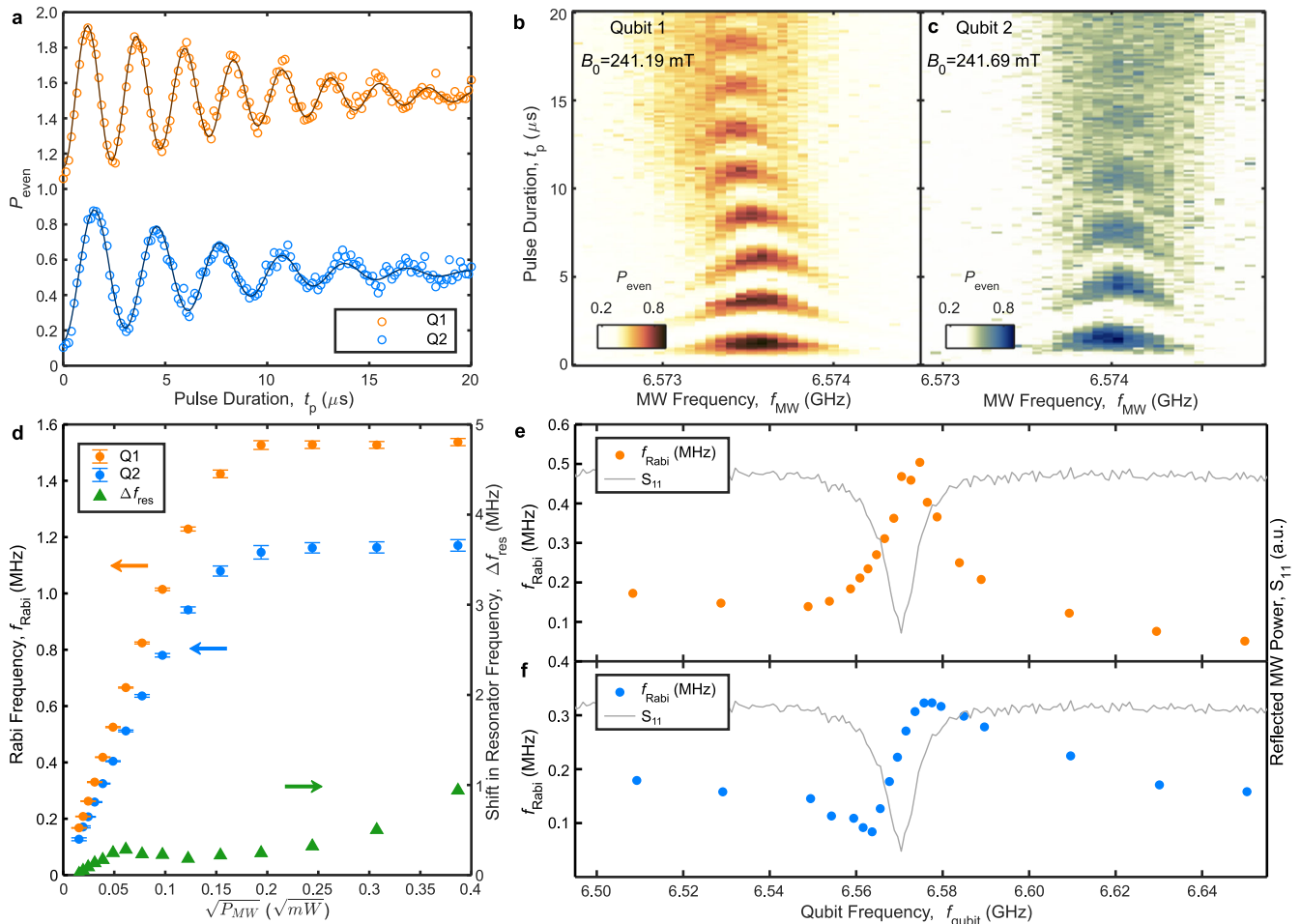


Fig. 2 Coherent control. **a** Coherent Rabi oscillations for both qubits. The Qubit 1 measurement is offset by 1.0 for clarity. **b, c** Rabi chevrons for Qubit 1 (**b**) and Qubit 2 (**c**). The DC magnetic field is tuned to shift the qubits close to the DR centre frequency. **d** Rabi frequency vs. MW power applied to the coaxial loop coupler. For low powers, the Rabi frequencies of both qubits are linearly proportional to the square root of the power, as expected (see text for more details). The Rabi frequencies begin to saturate at an input power of $\sim 20 \mu\text{W}$, as discussed in the text. We plot the shift in the DR frequency from its low-power value (green triangles) as a function of the applied microwave power, measured in a continuous wave experiment. **e, f** Rabi frequencies vs. qubit frequencies for Qubit 1 (**e**) and Qubit 2 (**f**). For each data point (solid circles), the DC magnetic field is tuned appropriately in order to shift the qubits to the desired frequency, then f_{Rabi} at that qubit frequency is measured. The error bars are not shown since they all lie within the extent of the data point markers. The DR S_{11} measurement from Fig. 1f is superimposed (grey line) on these panels for ease of comparison. The region of enhanced Rabi frequencies overlaps with the DR response, confirming that magnetic resonance via the KTO DR is the primary mechanism for driving spin rotations in these regions. Black solid lines are Lorentzian fits to the f_{Rabi} distributions.

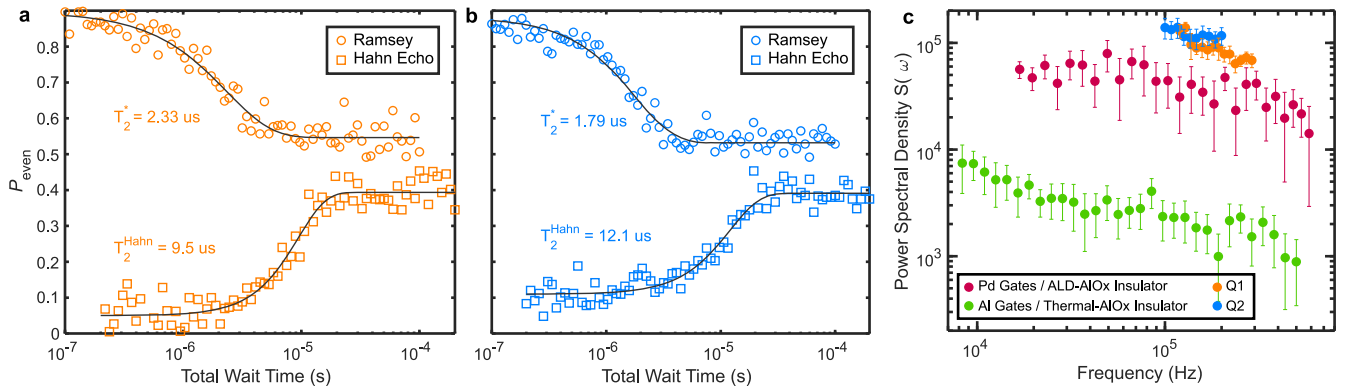


Fig. 3 Coherence time measurements. **a, b** Spin coherence times measured via Ramsey free induction decay (T_2^*) and Hahn echo (T_2^{Hahn}) experiments for Qubit 1 (**a**) and Qubit 2 (**b**). The Hahn echo data are offset by -0.1 for clarity. **c** CPMG noise spectroscopy measurements taken from three devices having a similar gate layout (Orange: Our device—Qubit 1, Blue: Our device, Qubit 2, Purple: Device A—Pd gate electrodes with an ALD- AlO_x insulator, Green: Device B—Al gate electrodes with a thermal- AlO_x insulator). $S(\omega)$ is the power spectral density of the qubit frequency noise. The error bars indicate the 95% confidence interval bounds for the $S(\omega)$ fits.

The reported spin coherence times are 1–2 orders of magnitude smaller than the best measured values in silicon MOS devices⁵. In order to determine if this is related to the DR, we make a comparison of the coherence and noise properties for typical silicon qubit devices constructed with palladium gates and aluminium gates. We first compare Carr-Purcell-Meiboom-Gill (CPMG) noise spectroscopy measurements⁴³ from our device and two other devices (one containing palladium gates and the other aluminium gates) having nearly identical gate layouts, but where the qubit control signals are delivered by conventional on-chip TLs (Fig. 3c). The TL device with Al gate electrodes (green circles) has a thermally grown AlO_x gate insulator, while the other TL device (purple circles) is made from exactly the same materials as the current device (Pd gates with an ALD- AlO_x insulator), whose noise spectroscopy data is also shown. The results demonstrate that the devices with Pd gate electrodes and ALD insulators have a similar noise floor, which is an order of magnitude higher than that of the Al gate device, despite the residual ^{29}Si concentration (50 ppm) being considerably lower in the Pd devices than the one containing Al gates (800 ppm). We note that the spectra obtained have a frequency dependency weaker than the charge-noise-induced $1/f$ trend. The frequency range reported here typically has a stronger white noise component due to instrumental thermal noise. The lower frequency range, however, would be expected to be dominated by $1/f$ noise created by charges in the oxide⁴⁴. We could not observe this effect due to the limited coherence time in our device, which sets the minimum frequency accessible by this technique. Comparing the T_2^{CPMG} times across all devices (see Supplementary Note 6) shows that the coherence of the Pd gate based qubits are all comparable and considerably reduced relative to the Al gate based qubits.

We believe that the higher decoherence of the qubits in the Pd devices is most likely related to the materials used, where charge noise arising from the ALD-grown AlO_x gate oxide layers⁴⁵ is a potential source. The slight difference in the noise power spectral densities of the Pd devices (with and without DR, see Fig. 3c) could be due to device variability, or perhaps because the oxide charges are disturbed in the DR experiment over a large area as compared to a small area in a conventional TL-based one. The variability in the coherence properties will be investigated in the future by measuring additional devices. Ultimately, we believe that moving to an Al device with thermally grown AlO_x should substantially improve the qubit coherence times.

DISCUSSION

We have demonstrated, for the first time, the coherent control of spin qubits in a nanoelectronic device using a globally applied magnetic field, achieving Rabi frequencies greater than 1 MHz for an input power of approximately $20 \mu\text{W}$. We also report a comparative analysis of the coherence and noise properties of devices where ESR is driven via on-chip transmission lines (local control) to those employing an off-chip dielectric resonator (global control). The coherence times of the local and global control devices made from identical materials (Pd gates with an ALD oxide) are within a factor of 3, but differ by an order of magnitude from that measured in a local control device made with an Al gate stack, leading us to suspect the device materials as the origin of noise. In future work, we plan to apply this off-chip DR control technique to a device made with Al gate electrodes and thermally grown AlO_x gate insulators, which we expect will result in longer spin coherence times.

Another avenue for improvement is the DR quality factor ($Q_i = 780$), which is currently limited by losses in the device. The material-limited quality factor for KTO DRs is approximately two orders of magnitude larger ($Q_i > 60,000$)²⁶—reaching this limit would mean the power could be reduced a hundredfold for a given B_1 amplitude, with corresponding lower levels of undesired

disturbance, for example due to unintended microwave loops or resonances in the device.

The improvements in global control hardware developed here should be accompanied by efforts to design and optimise pulse protocols for implementing high-fidelity single qubit gate operations⁴⁶. Such a protocol has already been experimentally demonstrated in a SiMOS spin qubit device equipped with on-chip TL control⁴⁷. In addition, qubit operations such as initialisation, readout and two-qubit entangling gates must be harmonised with the presence of the continuously driven microwave field generated by a high-Q resonator. Recent work in this direction⁴⁸ shows that high-fidelity gates should be possible with realistic experimental parameters.

Our work shows that delivering microwave signals to spin qubits in a quantum processor—something that has so far been seen as a major challenge and drawback of the platform—can be elegantly resolved by means of global control using a KTO dielectric resonator. Demonstrating off-chip coherent control of spin qubits brings the prospect of large-scale spin-based quantum computers one important step closer.

METHODS

Pulsing scheme for the ESR measurements

A diagram for the scheme is depicted in Fig. 1e, please refer to this figure for the following discussion. The DQD is initialised as a $|\downarrow\uparrow\rangle$ state in the (3,1) charge configuration point near the (3,1)–(4,0) transition. It is then pulsed deeper into the (3,1) region (square) and a square microwave pulse is applied to the dielectric resonator, generating an alternating magnetic field, B_1 , which can rotate the spins if they are in resonance with the field. Readout is performed in the Pauli Spin Blockade region (triangle) and reveals if the system is in an even or odd state (see the text for more detail). Finally, a diabatic ramp from (4,0) (circle) to (3,1) (star) is applied in order to both re-initialise the DQD in a $|\downarrow\uparrow\rangle$ state (see Supplementary Note 4) and implement gate-level feedback. The gate-level feedback protects the measurements from charge-noise-induced charge transition shifts by monitoring the transition during the ramp and applying a correction to the detuning (ϵ)⁶.

DATA AVAILABILITY

The data supporting the findings of this work are available from the corresponding authors upon reasonable request.

CODE AVAILABILITY

The codes supporting the findings of this work are available from the corresponding authors upon reasonable request.

Received: 1 July 2022; Accepted: 17 October 2022;

Published online: 04 November 2022

REFERENCES

- Preskill, J. Quantum computing in the NISQ era and beyond. *Quantum* **2**, 79 (2018).
- Shor, P. W. Algorithms for quantum computation: discrete logarithms and factoring. In *Proc. 35th annual symposium on foundations of computer science*, 124–134 (IEEE, 1994).
- Fowler, A. G., Mariantoni, M., Martinis, J. M. & Cleland, A. N. Surface codes: towards practical large-scale quantum computation. *Phys. Rev. A* **86**, 032324 (2012).
- Lekitsch, B. et al. Blueprint for a microwave trapped ion quantum computer. *Sci. Adv.* **3**, e1601540 (2017).
- Veldhorst, M. et al. An addressable quantum dot qubit with fault-tolerant control-fidelity. *Nat. Nanotechnol.* **9**, 981–985 (2014).
- Yang, C. H. et al. Operation of a silicon quantum processor unit cell above one kelvin. *Nature* **580**, 350–354 (2020).

7. Petit, L. et al. Universal quantum logic in hot silicon qubits. *Nature* **580**, 355–359 (2020).
8. Veldhorst, M., Eenink, H., Yang, C. & Dzurak, A. Silicon CMOS architecture for a spin-based quantum computer. *Nat. Commun.* **8**, 1766 (2017).
9. Hutin, L. et al. Si MOS technology for spin-based quantum computing. In *2018 48th European Solid-State Device Research Conference (ESSDERC)*, 12–17 (IEEE, 2018).
10. Yoneda, J. et al. A quantum-dot spin qubit with coherence limited by charge noise and fidelity higher than 99.9%. *Nat. Nanotechnol.* **13**, 102–106 (2018).
11. Yang, C. et al. Silicon qubit fidelities approaching incoherent noise limits via pulse engineering. *Nat. Electron.* **2**, 151–158 (2019).
12. Veldhorst, M. et al. A two-qubit logic gate in silicon. *Nature* **526**, 410–414 (2015).
13. Huang, W. et al. Fidelity benchmarks for two-qubit gates in silicon. *Nature* **569**, 532–536 (2019).
14. Xue, X. et al. Quantum logic with spin qubits crossing the surface code threshold. *Nature* **601**, 343–347 (2022).
15. Koppens, F. H. et al. Driven coherent oscillations of a single electron spin in a quantum dot. *Nature* **442**, 766–771 (2006).
16. Dehollain, J. P. et al. Nanoscale broadband transmission lines for spin qubit control. *Nanotechnology* **24**, 015202 (2013).
17. Nowack, K. C., Koppens, F., Nazarov, Y. V. & Vandersypen, L. Coherent control of a single electron spin with electric fields. *Science* **318**, 1430–1433 (2007).
18. Pioro-Ladriere, M. et al. Electrically driven single-electron spin resonance in a slanting Zeeman field. *Nat. Phys.* **4**, 776–779 (2008).
19. Kawakami, E. et al. Electrical control of a long-lived spin qubit in a Si/SiGe quantum dot. *Nat. Nanotechnol.* **9**, 666–670 (2014).
20. Takeda, K. et al. A fault-tolerant addressable spin qubit in a natural silicon quantum dot. *Sci. Adv.* **2**, e1600694 (2016).
21. Watson, T. et al. A programmable two-qubit quantum processor in silicon. *Nature* **555**, 633–637 (2018).
22. Li, R. et al. A crossbar network for silicon quantum dot qubits. *Sci. Adv.* **4**, eaar3960 (2018).
23. Struck, T. et al. Low-frequency spin qubit energy splitting noise in highly purified 28 Si/SiGe. *npj Quantum Inf.* **6**, 1–7 (2020).
24. Kane, B. E. A silicon-based nuclear spin quantum computer. *Nature* **393**, 133–137 (1998).
25. Hill, C. D. et al. A surface code quantum computer in silicon. *Sci. Adv.* **1**, e1500707 (2015).
26. Vahapoglu, E. et al. Single-electron spin resonance in a nanoelectronic device using a global field. *Sci. Adv.* **7**, eabg9158 (2021).
27. Laucht, A. et al. Electrically controlling single-spin qubits in a continuous microwave field. *Sci. Adv.* **1**, e1500022 (2015).
28. Blank, A., Stavitski, E., Levanon, H. & Gubaydullin, F. Transparent miniature dielectric resonator for electron paramagnetic resonance experiments. *Rev. Sci. Instrum.* **74**, 2853–2859 (2003).
29. Vallabhapurapu, H. H. et al. Fast coherent control of a nitrogen-vacancy-center spin ensemble using a KTaO₃ dielectric resonator at cryogenic temperatures. *Phys. Rev. Appl.* **16**, 044051 (2021).
30. Petta, J. R. et al. Coherent manipulation of coupled electron spins in semiconductor quantum dots. *Science* **309**, 2180–2184 (2005).
31. Pla, J. J. et al. A single-atom electron spin qubit in silicon. *Nature* **489**, 541–544 (2012).
32. Muhonen, J. T. et al. Storing quantum information for 30 seconds in a nanoelectronic device. *Nat. Nanotechnol.* **9**, 986–991 (2014).
33. Brauns, M., Amitonov, S. V., Spruijtenburg, P.-C. & Zwanenburg, F. A. Palladium gates for reproducible quantum dots in silicon. *Sci. Rep.* **8**, 1–8 (2018).
34. Yang, C. H., Lim, W. H., Zwanenburg, F. A. & Dzurak, A. S. Dynamically controlled charge sensing of a few-electron silicon quantum dot. *AIP Adv.* **1**, 042111 (2011).
35. Leon, R. C. et al. Coherent spin control of s-, p-, d- and f-electrons in a silicon quantum dot. *Nat. Commun.* **11**, 797 (2020).
36. Seedhouse, A. E. et al. Pauli blockade in silicon quantum dots with spin-orbit control. *PRX Quantum* **2**, 010303 (2021).
37. Saraiva, A. et al. Materials for silicon quantum dots and their impact on electron spin qubits. *Adv. Funct. Mater.* **32**, 2105488 (2022).
38. Zwerfer, A. et al. Qubits made by advanced semiconductor manufacturing. *Nat. Electron.* **5**, 184–190 (2022).
39. Undseth, B. et al. Nonlinear response and crosstalk of strongly driven silicon spin qubits. Preprint at <https://arxiv.org/abs/2205.04905> (2022).
40. Huang, W., Veldhorst, M., Zimmerman, N. M., Dzurak, A. S. & Culcer, D. Electrically driven spin qubit based on valley mixing. *Phys. Rev. B* **95**, 075403 (2017).
41. Gilbert, W. et al. On-demand electrical control of spin qubits. Preprint at <https://arxiv.org/abs/2201.06679> (2022).
42. Paladino, E., Galperin, Y. M., Falcì, G. & Altshuler, B. L. 1/f noise: Implications for solid-state quantum information. *Rev. Mod. Phys.* **86**, 361–418 (2014).
43. Álvarez, G. A. & Suter, D. Measuring the spectrum of colored noise by dynamical decoupling. *Phys. Rev. Lett.* **107**, 230501 (2011).
44. Chan, K. et al. Assessment of a silicon quantum dot spin qubit environment via noise spectroscopy. *Phys. Rev. Appl.* **10**, 044017 (2018).
45. Connors, E. J., Nelson, J., Qiao, H., Edge, L. F. & Nichol, J. M. Low-frequency charge noise in si/sige quantum dots. *Phys. Rev. B* **100**, 165305 (2019).
46. Hansen, I. et al. Pulse engineering of a global field for robust and universal quantum computation. *Phys. Rev. A* **104**, 062415 (2021).
47. Hansen, I. et al. Implementation of an advanced dressing protocol for global qubit control in silicon. *Appl. Phys. Rev.* **9**, 031409 (2022).
48. Seedhouse, A. E. et al. Quantum computation protocol for dressed spins in a global field. *Phys. Rev. B* **104**, 235411 (2021).

ACKNOWLEDGEMENTS

We acknowledge support from the Australian Research Council (DE190101397, FL190100167 and CE170100012), the US Army Research Office (W911NF-17-1-0198) and the NSW Node of the Australian National Fabrication Facility. The views and conclusions contained in this document are those of the authors and should not be interpreted as representing the official policies, either expressed or implied, of the Army Research Office or the US Government. E.V. and J.P.S.-S. acknowledge support from Sydney Quantum Academy. We thank Peter Becker for the preparation of the isotopically purified silicon substrate.

AUTHOR CONTRIBUTIONS

E.V. and J.P.S.-S. performed the experiments. J.P.S.-S. and J.J.P. designed and fabricated the DR. T.D. designed the sample enclosure and assisted with the DR characterisation. W.H.L. and F.E.H. fabricated the silicon device. M.L.W.T., N.V.A. and H.-J.P. prepared and characterised the isotopically purified silicon substrate. E.V., J.P.S.-S., R.C.C.L., J.D.C. and A.S. analysed the data. C.H.Y., T.T., A.L. and A.S. contributed to discussions on the experimental results. E.V., J.P.S.-S., J.J.P. and A.S.D. wrote the manuscript with input from all authors. J.J.P. and A.S.D. supervised the project, and contributed equally to this work.

COMPETING INTERESTS

J.J.P. and A.S.D. are inventors on a patent related to this work filed by the University of New South Wales with a priority date of 15 November 2019. A.S.D. is also CEO and a director of Diraq Pty Ltd. The remaining authors declare no competing interests.

ADDITIONAL INFORMATION

Supplementary information The online version contains supplementary material available at <https://doi.org/10.1038/s41534-022-00645-w>.

Correspondence and requests for materials should be addressed to E. Vahapoglu, J. P. Slack-Smith, A. S. Dzurak or J. J. Pla.

Reprints and permission information is available at <http://www.nature.com/reprints>

Publisher's note Springer Nature remains neutral with regard to jurisdictional claims in published maps and institutional affiliations.



Open Access This article is licensed under a Creative Commons Attribution 4.0 International License, which permits use, sharing, adaptation, distribution and reproduction in any medium or format, as long as you give appropriate credit to the original author(s) and the source, provide a link to the Creative Commons license, and indicate if changes were made. The images or other third party material in this article are included in the article's Creative Commons license, unless indicated otherwise in a credit line to the material. If material is not included in the article's Creative Commons license and your intended use is not permitted by statutory regulation or exceeds the permitted use, you will need to obtain permission directly from the copyright holder. To view a copy of this license, visit <http://creativecommons.org/licenses/by/4.0/>.

© The Author(s) 2022